Calculation of fine-structure effects in O^+-O collisions

A. P. Hickman, M. Medikeri-Naphade, and C. D. Chapin
Department of Physics, Lehigh University, Bethlehem, Pennsylvania 18015

D. L. Huestis
Molecular Physics Laboratory, SRI International, Menlo Park, California 94025

(Received 24 February 1997)

Effects of the fine structure of atomic oxygen on collisions of O with O^+ have been investigated theoretically. The starting point of the analysis was a set of potential curves for $O_2{}^+$ calculated in LS coupling. Potential curves and matrix elements were derived that include spin-orbit effects and properly dissociate to the three asymptotic limits O^+-$O(^3P_J)$ $(J=2,1,0)$. Quantum-mechanical, coupled-channel scattering calculations were performed to determine inelastic, charge-exchange and momentum-transfer (diffusion) cross sections in the energy range 0.002–1.9 eV. The results exhibit a strong dependence on the initial fine-structure level. For example, the momentum-transfer cross sections are typically about 50% larger for the initial level $J=2$ than for $J=1$ or 0. A weighted average of the present cross sections, appropriate for a statistical distribution of fine-structure levels, can be compared with previous results based on performing uncoupled, single-channel calculations. The comparison confirms the accuracy of the single-channel model as long as the collision energy is greater than about 0.03 eV. For lower energies, the single-channel model overestimates the cross sections. The problem arises because angular momentum coupling effects lead to considerable cancellation of the charge-quadrupole terms in the asymptotic interaction potentials. As the collision energy decreases, these terms become increasingly important. [S1050-2947(97)09011-2]

PACS number(s): 34.50.Pi, 34.20.−b

I. INTRODUCTION

The scattering of O^+ and O is one of the most important collision processes in the upper atmosphere. The diffusion of O^+ in O plays a crucial role in models of global wind circulation and in determining the ion density in the ionosphere. The importance of the scattering process has stimulated several theoretical calculations, but there have been persistant discrepancies between theoretical results and information inferred from experiments.

The quantities that have been calculated or measured most frequently for this system are the charge-exchange and momentum-transfer cross sections. Early calculations were performed by Dalgarno [1,2], Knof, Mason, and Vanderslice [3], Banks [4], Stubbe [5], and Schunk and Walker [6]. Most recent theoretical calculations [7,8] have been based on the potential curves calculated by Stallcop, Partridge, and Levin [7], although other potentials [9] are available. A preliminary account of the present work has recently appeared [10].

Only two groups [11,12] have reported laboratory data for O^+-O collisions. These experiments were performed at collision energies of several keV, far above the range appropriate for atmospheric applications. However, several studies [13–17] based on the analysis of observations of the upper atmosphere have inferred values of an averaged cross section that can be compared with calculations. Until recently, all of these studies led to values larger than the predictions of theory, by factors of about 1.3. A discrepancy of that size was troubling, considering the importance of the O^+-O scattering to so many atmospheric models. More recent work [16,17] analyzing the observations has led to smaller cross sections and a reduced discrepancy with theoretical calculations.

The discrepancies between previous calculations and the available data led us to consider whether significant effects might have been omitted from the theoretical analysis. Considerable simplification of the previous calculations was achieved by assuming that the fine-structure energy levels were degenerate. The actual splittings are on the order of $100-200\ \mathrm{cm}^{-1}$, which corresponds to kT for $T\sim 300$ K. Since the range of temperatures important for atmospheric applications is $T\sim 300-2000$ K, the fine-structure splitting appears large enough to have an effect.

The neglect of fine-structure effects leads to an analysis of the scattering based on several separate, single-channel calculations. When LS coupling is used to describe the interaction of $O^+(^4S)$ with $O(^3P)$, the resulting $O_2{}^+$ molecule has 24 distinct electronic states denoted by $^{2S+1}\Lambda^q$, where $S=\frac{1}{2},\frac{3}{2},\frac{5}{2}$ (corresponding to doublets, quartets, sextets), $\Lambda=0,1$ (corresponding to Σ, Π), and $q=g,u$ (gerade, ungerade). Neglecting the rotational coupling between these states during the collision, one can formulate the dynamics entirely in terms of the phase shifts for single-channel scattering on each potential curve separately. The calculations for each g-u pair ($^{2S+1}\Lambda^g$ and $^{2S+1}\Lambda^u$) are combined to form momentum-transfer or charge-exchange cross sections, and then these cross sections are averaged over the possible electronic states.

Introducing the finite splitting of the fine-structure levels naturally complicates the collision dynamics. There are then several possible energy levels of the system, and one must implement a coupled-channel approach to handle the transitions among the various levels. It is also necessary to formulate the momentum-transfer and charge-exchange cross sections in terms of T matrix elements instead of scattering phase shifts.

This paper is organized as follows. Section II discusses the calculation of adiabatic molecular potential curves that incorporate fine-structure effects. The technique implemented is a generalization of previous work [18] that allows us to start with the available molecular potential curves (calculated in LS coupling) and then add spin-orbit effects. Section III discusses the formulation of the coupled-channel scattering dynamics. Results are discussed in Sec. IV, and Sec. V contains concluding remarks.

II. MOLECULAR POTENTIAL CURVES

The calculations require molecular potential curves and matrix elements for O_2^+ that include spin-orbit effects. We determine this information using a generalization of a method developed by Cohen and Schneider [18]. This section briefly describes the analysis. The Hamiltonian $H(R)$ at each internuclear separation R consists of an electronic component and a spin-orbit component:

$$H(R)=H_{\rm el}+H_{\rm so}. \tag{1}$$

Potentials calculated using standard electronic structure codes, such as the electronic potentials of Stallcop, Partridge, and Levin [7], provide information about $H_{\rm el}$, but no information about $H_{\rm so}$. Information about $H_{\rm so}$ available from spectroscopy can be combined with the electronic potentials to obtain the necessary matrix elements of the full $H(R)$.

The available potential curves [7] provide matrix elements of $H_{\rm el}$ in a set of states corresponding to particular values of the molecule's angular momentum quantum numbers in the LS coupling scheme. For the O_2^+ molecule, we denote the electronic, spin, and total angular momentum by $\mathbf{L}_{\rm O}$, $\mathbf{S}_{\rm O}$, and $\mathbf{J}$, and the spin of O^+ by $\mathbf{S}_+$. Then the LS coupling scheme is

$$\mathbf{L}_{\rm O}=\mathbf{L}, \quad \mathbf{S}_{\rm O}+\mathbf{S}_+=\mathbf{S}.$$

Following Durup [19], we use the notation $|LS\Lambda\Omega\rangle$ to denote the states in this coupling scheme. L, the total orbital angular momentum quantum number, is 1 for the ground electronic state of $O(^3P)$. Λ gives the projection of $\mathbf{L}$ on the internuclear axis, and has the value 0 for Σ states and 1 for Π states. S is the total spin quantum number. Each Σ or Π state may be a doublet ($S=\frac{1}{2}$), a quartet ($S=\frac{3}{2}$), or a sextet ($S=\frac{5}{2}$). Ω is the projection of $\mathbf{L}+\mathbf{S}$ on the internuclear axis. All electronic states are also denoted either gerade or ungerade, but we will suppress this notation since the present section applies equally to either symmetry. The matrix elements of $H_{\rm el}(R)$ in the states $|LS\Lambda\Omega\rangle$ are given by

$$\langle LS'\Lambda'\Omega'|H_{\rm el}(R)|LS\Lambda\Omega\rangle=\delta_{S'S}\delta_{\Lambda'\Lambda}\delta_{\Omega\Omega'}V_{S\Lambda}(R). \tag{2}$$

The functions $V_{S\Lambda}(R)$ are the potential curves [7] for the states $^{2S+1}\Lambda$ defined above for O_2^+.

We also need the matrix elements of $H_{\rm so}$. In the asymptotic limit ($R\rightarrow\infty$), these matrix elements may be determined from spectroscopic data. We then assume that $H_{\rm so}$ is independent of R. Our results provide justification, *a posteriori*, for this approximation. It turns out that the cross sections are insensitive to the details of $H_{\rm so}$ in the region of small R where the approximation might break down.

TABLE I. Energy levels of $O(^3P_J)$.

J	E_J (cm^{-1})	E_J (eV)	E_J (a.u.)
2	0	0	0
1	158.5	0.01965	7.222×10^{-4}
0	226.5	0.02808	10.32×10^{-4}

The matrix elements of $H_{\rm so}$ are most easily determined in a set of states corresponding to a different angular momentum coupling scheme. This scheme is

$$\mathbf{L}_{\rm O}+\mathbf{S}_{\rm O}=\mathbf{J}, \quad \mathbf{J}+\mathbf{S}_+=\mathbf{K}.$$

Writing the corresponding states $|JK\Omega\rangle$, we have

$$\langle J'K'\Omega'|H_{\rm so}|JK\Omega\rangle=\delta_{J'J}\delta_{K'K}\delta_{\Omega'\Omega}E_J, \tag{3}$$

where E_J denotes the energy of the atomic oxygen ^3P_J level. The values of E_J are available in the literature [20] and are given in Table I.

Equations (2) and (3) provide the eigenvalues and eigenvectors, separately, of the operators $H_{\rm el}(R)$ and $H_{\rm so}$. In order to evaluate explicitly the matrix elements of $H(R)$, we must write the matrix elements of $H_{\rm el}(R)$ and $H_{\rm so}$ in a common basis set. For the scattering calculations, it is convenient to choose the $|JK\Omega\rangle$ basis. Using standard techniques of angular momentum algebra [21], it can be shown that the $|JK\Omega\rangle$ basis is related to the $|LS\Lambda\Omega\rangle$ basis by the following unitary transformation:

$$\langle LS\Lambda\Omega'|JK\Omega\rangle=\delta_{\Omega'\Omega}(-1)^{S+S_{\rm O}+S_++K-\Omega}\times\sqrt{(2K+1)(2S+1)(2J+1)}\times\begin{Bmatrix}L & S & K\\ S_+ & J & S_{\rm O}\end{Bmatrix}\begin{pmatrix}L & S & K\\ \Lambda & \Omega-\Lambda & -\Omega\end{pmatrix}. \tag{4}$$

$\{\}$ and $()$ refer to 6-j and 3-j coefficients, respectively [21].

By using Eq. (4) to express the $|JK\Omega\rangle$ states in terms of the $|LS\Lambda\Omega\rangle$ states, we can evaluate the matrix elements $\langle J'K'\Omega'|H_{\rm el}|JK\Omega\rangle$. We then have all the matrix elements of $H(R)$ in the $|JK\Omega\rangle$ basis. This matrix, $\langle J'K'\Omega'|H(R)|JK\Omega\rangle$, has both diagonal and off-diagonal terms and contains all the information needed to describe elastic and inelastic scattering and charge exchange involving the fine-structure states of atomic O and O^+.

Adiabatic potential curves that include fine structure are obtained by evaluating the eigenvalues of the matrix $\langle J'K'\Omega'|H(R)|JK\Omega\rangle$ as a function of R. These curves are shown in Figs. 1–4. Since $H(R)$ is already diagonal in Ω, we show a separate set of curves of each value of Ω. The limiting behavior of these curves at small and large R can be understood as follows. For small values of R, the magnitudes of the $V_{S\Lambda}(R)$ are much larger than the fine-structure energy level splittings, and $H_{\rm so}$ may be regarded as a small perturbation. In this limit each curve becomes approximately equal to one of the $V_{S\Lambda}(R)$. As $R\rightarrow\infty$, all matrix elements of

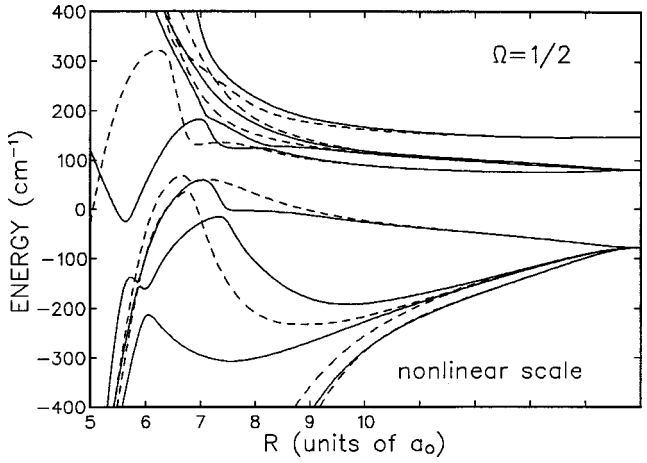

FIG. 1. Adiabatic potential curves for $\Omega=\frac{1}{2}$. The solid (dashed) lines are for the gerade (ungerade) curves. The labels $J=2$, 1, and 0 denote the asymptotic limits corresponding to $O(^3P_J)$-O^+. Note the scale is nonlinear for $R>10a_0$.

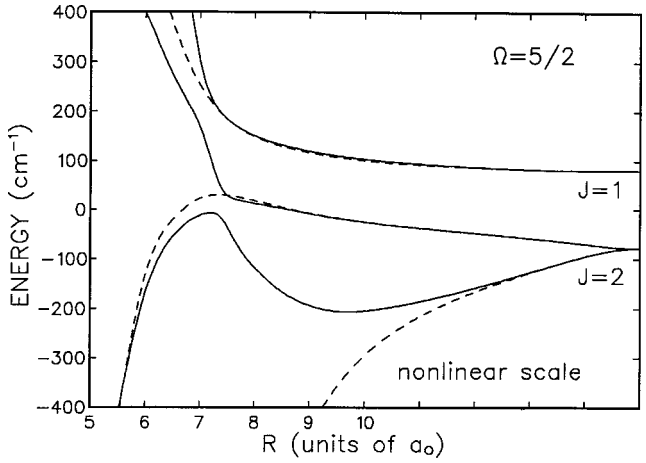

FIG. 3. Adiabatic potential curves for $\Omega=\frac{5}{2}$. The solid (dashed) lines are for the gerade (ungerade) curves. The labels $J=2$ and 1 denote the asymptotic limits corresponding to $O(^3P_J)$-O^+. Note the scale is nonlinear for $R>10a_0$.

$H_{el}(R)$ [that is, the $V_{S\Lambda}(R)$] approach 0; in this limit the adiabatic energies are determined entirely by H_{so} and are just the fine-structure energy levels of atomic O. Asymptotically, then, each potential curve approaches one of the three fine-structure levels of atomic O. In contrast, the original curves of Stallcop, Partridge, and Levin [7] are all degenerate asymptotically.

III. SCATTERING FORMALISM

A. Single-channel theory

We begin by summarizing the single-channel formalism for charge-exchange and momentum-transfer (diffusion) collisions of homonuclear diatomic ions. We present the results in a manner that clearly exhibits how the extension to the coupled-channel case is carried out. In the single-channel limit, each g-u pair of potential curves is treated separately. Using the present notation, such a pair for O_2^+ would be $V^g_{S\Lambda}(R)$ and $V^u_{S\Lambda}(R)$. The phase shifts $\eta^{lg}_{S\Lambda}$ and $\eta^{lu}_{S\Lambda}$ for each of these potentials can be calculated separately. Then the charge-exchange and diffusion cross sections for the $S\Lambda$ states are given by

$$Q^{S\Lambda}_{ex}(E)=\frac{\pi}{k^2}\sum_l (2l+1)\sin^2(\eta^{lg}_{S\Lambda}-\eta^{lu}_{S\Lambda}) \tag{5}$$

and

$$Q^{S\Lambda}_{D}(E)=\frac{4\pi}{k^2}\sum_l (l+1)\sin^2(\eta^{l,g\text{-}u}_{S\Lambda}-\eta^{l+1,u\text{-}g}_{S\Lambda}), \tag{6}$$

where $k^2=2\mu E/\hbar^2$, and μ is the reduced mass. The notation g-u and u-g in the phase shifts means that either g or u is taken according to whether l is even or odd, and whether Λ denotes a Σ or Π state. This effect arises from the quantum-mechanical indistinguishability of the nuclei (nuclear symmetry). For the detailed formulas, which depend on the nuclear spin, the reader is referred to the literature [1,7,22]. Mason and McDaniel [22] have noted that the nuclear sym-

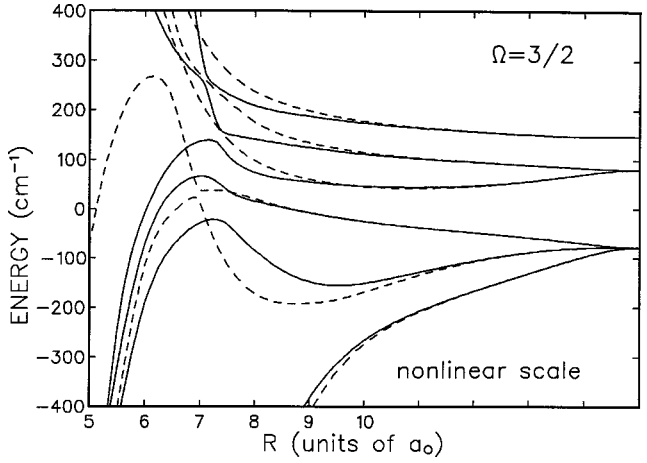

FIG. 2. Adiabatic potential curves for $\Omega=\frac{3}{2}$. The solid (dashed) lines are for the gerade (ungerade) curves. The labels $J=2$, 1, and 0 denote the asymptotic limits corresponding to $O(^3P_J)$-O^+. Note the scale is nonlinear for $R>10a_0$.

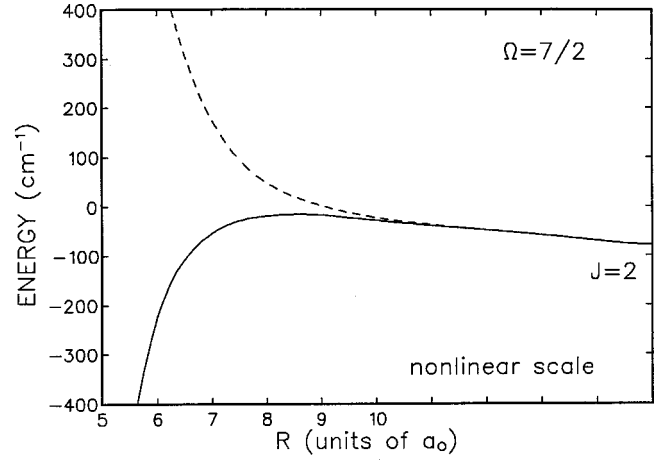

FIG. 4. Adiabatic potential curves for $\Omega=\frac{7}{2}$. The solid (dashed) lines are for the gerade (ungerade) curves. The label $J=2$ denotes the asymptotic limits to $O(^3P_2)$-O^+. Note the scale is nonlinear for $R>10a_0$.

metry effect is very small for the energies we consider. They rearranged Eq. (6) to yield a term independent of nuclear symmetry, plus a small correction. This symmetrized version of Eq. (6) is

$$Q_D^{S\Lambda}(E)=\frac{2\pi}{k^2}\sum_l\ (l+1)[\sin^2(\eta_{S\Lambda}^{lg}-\eta_{S\Lambda}^{l+1,u})+(g\leftrightarrow u)]$$
$$+\text{nuclear symmetry terms}, \tag{7}$$

where the notation $(g\leftrightarrow u)$ denotes a second term in which g and u are interchanged. In Sec. IV B we present numerical calculations confirming the small size of the nuclear symmetry terms.

The total momentum-transfer cross section is a weighted sum of the $Q_D^{S\Lambda}$. We can write the general expression

$$Q_D(E)=\frac{1}{N}\sum_{\Lambda=0}^{1}\sum_{S=1/2}^{5/2} g_{S\Lambda}Q_D^{S\Lambda}(E), \tag{8}$$

where $g_{S\Lambda}=(2-\delta_{\Lambda 0})(2S+1)$ is the degeneracy of each of the $S\Lambda$ levels, and the total number of states is $N=36$.

Equations (5) and (6) are derived by writing the differential cross section in terms of T matrix elements, which are related to the phase shifts by

$$T_{S\Lambda}^{lq}=1-\exp(2i\eta_{S\Lambda}^{lq})\quad (q=g\ \text{ or }\ u). \tag{9}$$

The expressions for $Q_D^{S\Lambda}$ and $Q_{\rm ex}^{S\Lambda}$ in terms of the T matrix elements are given below:

$$Q_{\rm ex}^{S\Lambda}(E)=\frac{\pi}{4k^2}\sum_l\ (2l+1)|T_{S\Lambda}^{lg}-T_{S\Lambda}^{lu}|^2, \tag{10}$$

$$Q_D^{S\Lambda}(E)=\frac{\pi}{2k^2}\sum_l\ [(2l+1)|T_{S\Lambda}^{lg}|^2-(l+1)T_{S\Lambda}^{lg}(T_{S\Lambda}^{l+1,u})^*$$
$$-lT_{S\Lambda}^{lg}(T_{S\Lambda}^{l-1,u})^*+(g\leftrightarrow u)]$$
$$+\text{nuclear symmetry terms}, \tag{11}$$

where $(\ )^*$ denotes the complex conjugate. These expressions can be reduced, after some algebra, to the phase shift expressions [Eqs. (5) and (6)] for the single-channel case. However, for the coupled-channel case, the T matrix formulation must be used.

An important difference between the expressions for $Q_{\rm ex}$ and Q_D concerns the convergence properties. For the O_2^+ system, the difference between a g-u pair of potentials becomes small exponentially as $R\to\infty$. Therefore for large l the sum in Eq. (5) or Eq. (10) converges rapidly because the difference between the g and u terms for the same l approaches zero. In contrast, Q_D mixes g and u phase shifts for different l, and the contributions to the sums in Eqs. [6] and [11] converge much more slowly with l.

Considerations of convergence are important for the O_2^+ system because the potentials are very long range. As $R\to\infty$, the leading terms behave as R^{-3} due to the electrostatic charge-quadrupole interaction [23], and two additional terms were included [7]:

$$V_{S\Lambda}(R)\to C_3R^{-3}+C_4R^{-4}+C_5R^{-5}. \tag{12}$$

TABLE II. Coefficients (in atomic units) determining the long range behavior of the LS potential curves.

Symmetry	C_3	C_4	C_5
Σ	−0.8	−2.55	13.0
Π	0.4	−2.55	9.6

The values of C_3, C_4, and C_5 are given in Table II. (These coefficients were obtained from the authors of Ref. [7]). Note that the C_n are the same for any g-u pair. The effect of the R^{-3} term in the potential is that the sum over l in Eq. (6) is very slowly convergent. To facilitate the evaluation of this sum, we calculated the phase shifts numerically for each l up to some value $l_{\rm max}$ and then invoked the Born approximation for $l>l_{\rm max}$. For l sufficiently large, the g and u phase shifts are nearly equal and can be obtained from the Born approximation for inverse power law potentials. The result [24] is

$$\eta_{\rm Born}^l=-\frac{\mu C_3k}{\hbar^2l(l+1)}-\frac{\pi\mu C_4k^2}{4\hbar^2(l-\frac{1}{2})(l+\frac{1}{2})(l+\frac{3}{2})}$$
$$-\frac{2\mu C_5k^3}{3\hbar^2(l-1)l(l+1)(l+2)}, \tag{13}$$

where we drop the subscript $S\Lambda$ since the analysis does not depend on it. We verified that the numerically calculated phase shifts approached the Born formula. The terms in Eq. (6) for $l>l_{\rm max}$ are approximated by an integral:

$$\sum_{l=l_{\rm max}+1}^{\infty}(l+1)\sin^2(\eta^l-\eta^{l+1})$$
$$\simeq\int_{l_{\rm max}+1/2}^{\infty}(l+1)\sin^2(\eta_{\rm Born}^l-\eta_{\rm Born}^{l+1})dl, \tag{14}$$

where the Born phase shifts are regarded as continuous functions of l. A change of variable to $y=(l_{\rm max}+\frac{1}{2})/l+1/2)$ converts the right hand side of Eq. (14) into an integral from 0 to 1 that can be evaluated by a low order Gaussian quadrature.

B. Coupled-channel theory

This section describes the formulation of the coupled-channel equations and the calculation of the cross sections. The coupled equations are set up in a standard fashion, and we will refer the reader to the literature for many of the details. The definitions of the charge-exchange and diffusion cross sections for O^+-O collisions in terms of the T matrix elements for the coupled-channel system will be presented in greater detail.

We consider the channels in both space-fixed (SF) and body-fixed (BF) frames. Our analysis follows that of Walker and Light [25]. In the SF frame, we define the states by extending the angular momentum coupling scheme based on the $|JK\Omega\rangle$ states defined in the preceding section. We define

$$\boldsymbol{l}+\mathbf{K}=\mathbf{P}, \tag{15}$$

where $\boldsymbol{l}$ is the orbital angular momentum of the O^+-O motion, $\mathbf{K}$ is the internal angular momentum of O_2^+, and $\mathbf{P}$ is

the grand total angular momentum. The SF states are denoted by $|JK\Omega l\rangle$. These states split into two uncoupled sets according to whether $(-1)^{l+P+K}=\pm 1$. The plus or minus denotes whether the total wave function changes sign when reflected in the scattering plane.

In the BF frame, the corresponding states will be labeled $|JK\Omega\pm\rangle$, where, as usual, we take linear combinations of the states with Ω and $-\Omega$.

$$|JK\Omega\pm\rangle=\frac{1}{\sqrt{2}}[|JK\Omega\rangle\pm|JK(-\Omega)\rangle]. \tag{16}$$

It should be understood that $\Omega>0$ in the above equation. The BF states are therefore also split into two sets according to the $\pm$ symmetry, and the two sets correspond exactly to the two sets defined above in the SF frame. The following matrix elements define the unitary transformation relating the BF and SF states:

$$\langle PJK\Omega\pm|PJKl\pm\rangle=(-1)^{P+l+\Omega}\sqrt{2(2l+1)}\times\begin{pmatrix} l & K & P \\ 0 & \Omega & -\Omega \end{pmatrix}. \tag{17}$$

Note that the $+$BF states only connect with the $+$SF states, and similarly for the $-$ states. This symmetry block diagonalizes the coupled equations.

We consider now the evaluation of the matrix elements of the Hamiltonian $H(R)$ in the BF frame. Applying Eqs. (2) and (4) from Sec. II, it can be shown that the matrix elements of the electronic Hamiltonian are

$$\langle J'K'\Omega\pm|H_{\rm el}(R)|JK\Omega\pm\rangle=\sum_{S\Lambda}\Gamma^{S\Lambda\Omega}_{J'K',JK}V_{S\Lambda}(R), \tag{18}$$

where

$$\Gamma^{S\Lambda\Omega}_{J'K',JK}=h_{KK'}(2S+1)\times\sqrt{(2K+1)(2K'+1)(2J+1)(2J'+1)}\times\begin{pmatrix} L & S & K' \\ \Lambda & \Omega-\Lambda & -\Omega \end{pmatrix}\begin{pmatrix} L & S & K \\ \Lambda & \Omega-\Lambda & -\Omega \end{pmatrix}\times\begin{Bmatrix} L & S & K' \\ S_+ & J' & S_{\rm O} \end{Bmatrix}\begin{Bmatrix} L & S & K \\ S_+ & J & S_{\rm O} \end{Bmatrix}, \tag{19}$$

where $h_{KK'}=1$ if $K-K'=0$, and $h_{KK'}=0$ otherwise, and again Ω is taken to be positive. The matrix elements of the spin-orbit component $H_{\rm so}$ are diagonal [Eq. (3)], and the centrifugal matrix elements can be easily obtained from the work of Launay [26].

The above analysis leads to four sets of 18 coupled equations: one set of 18 for each of the $+$ and $-$ symmetries for the gerade states, and again for the ungerade states. From the asymptotic behavior of the solutions we determine the T matrix elements, which are written $T^{Pq}_{JKl\to J'K'l'}$, ($q=g$ or u). We do not include the $\pm$ notation in the T matrix elements since any $l\to l'$ transition can be specified. The appropriate blocks of the T matrix are calculated separately for each P and q, and then $T^{Pq}_{JKl\to J'K'l'}$ is set to zero unless $(-1)^{l+K}=(-1)^{l'+K'}$.

The calculated T matrix elements can be used to determine elastic, inelastic, charge-exchange, and diffusion cross sections. For the diffusion cross sections, the appropriate formulas can be adapted from the analysis of Arthurs and Dalgarno [27] by noting that K, l, and P in the present paper correspond to j, l, and J in Ref. [27]. We also adopt the symmetrized treatment of g and u T matrix elements described in the preceding section, and thereby neglect the small nuclear symmetry effect for the diffusion cross sections. The g and u dependence of the results is obtained by using g for T matrix elements that depend on l and u for T matrix elements that depend on $l\pm 1$. The final result is the average of this term and the $(g\leftrightarrow u)$ term.

The elastic, inelastic, diffusion, and charge-exchange cross sections can be defined as sums of partial cross sections that depend on the total angular momentum quantum number P. We also sum over the internal quantum numbers in order to obtain cross sections for specific $J\to J'$ transitions. We obtain

$$Q_D^{J\to J'}=\sum_{P=1/2}^{\infty}(Q_D^{J\to J'})^P \tag{20}$$

and similar formulas for $Q_{\rm ex}^{J\to J'}$ and $Q^{J\to J'}$ in terms of $(Q_{\rm ex}^{J\to J'})^P$ and $(Q^{J\to J'})^P$. We consider first the diffusion cross section, which is defined by

$$Q_D^{J\to J'}=2\pi\int_0^{\pi}\frac{d\sigma^{J\to J'}}{d\theta}(1-\cos\theta)\sin\theta\,d\theta. \tag{21}$$

In order to evaluate this expression, we use the Legendre polynomial expansion

$$\frac{d\sigma^{J\to J'}}{d\theta}=\frac{\pi}{(2S_++1)(2J+1)k_J^2}\sum_{\lambda=0}^{\infty}\overline{A_\lambda}(J,J')P_\lambda(\cos\theta). \tag{22}$$

Explicit expressions for the $\overline{A}$ coefficients are obtained from the work of Hickman and Smith [28], who showed that one can express them as a single sum over P. This result enables us to relate the partial cross sections to terms of the form $\overline{A_\lambda^P}(J,J')$. With minor modification, we can adopt the explicit expressions given in Ref. [28]. The result is

$$(Q^{J\to J'})^P=\frac{\pi}{(2S_++1)(2J+1)k_J^2}\overline{A_0^P}(J,J') \tag{23}$$

and

$$(Q_D^{J\to J'})^P=\frac{\pi}{(2S_++1)(2J+1)k_J^2}[\overline{A_0^P}(J,J')-\tfrac{1}{3}\overline{A_1^P}(J,J')]. \tag{24}$$

Explicit expressions for the $\overline{A_\lambda}(J,J')$ are

$$\overline{A_0^P}(J,J')=\frac{2P+1}{2}\sum_{K=|J-S_+|}^{J+S_+}\sum_{l=|P-K|}^{P+K}\sum_{K'=|J'-S_+|}^{J'+S_+}\sum_{l'=|P-K'|}^{P+K'}\times[|T^{Pg}_{JKl\to J'K'l'}|^2+(g\leftrightarrow u)] \tag{25}$$

and

$$\overline{A_1^P}(J,J')=\mathrm{Re}\sum_{K=|J-S_+|}^{J+S_+}\sum_{l=|P-K|}^{P+K}\sum_{K'=|J'-S_+|}^{J'+S_+}\sum_{l'=|P-K'|}^{P+K'}\times[G^P(JKl,J'K'l')+H^P(JKl,J'K'l')], \tag{26}$$

where

$$G^P(JKl,J'K'l')=\tfrac{1}{2}\sum_{\lambda=l\pm1}\sum_{\lambda'=l'\pm1}Z(l,P,\lambda,P;K,1)\times Z(l',P,\lambda',P;K',1)\times[T^{Pg}_{JKl\to J'K'l'}(T^{Pu}_{JK\lambda\to J'K'\lambda'})^*+(g\leftrightarrow u)], \tag{27}$$

and

$$\begin{aligned}H^P(JKl,J'K'l')&=\tfrac{1}{2}\sum_{\lambda=l\pm1}\sum_{\lambda'=l'\pm1}[Z(l,P,\lambda,P-1;K,1)\\&\times Z(l',P,\lambda',P-1;K',1)\\&\times T^{Pg}_{JKl\to J'K'l'}(T^{P-1,u}_{JK\lambda\to J'K'\lambda'})^*\\&+Z(l,P,\lambda,P+1;K,1)Z(l',P,\lambda',P+1;K',1)\\&\times T^{Pg}_{JKl\to J'K'l'}(T^{P+1,u}_{JK\lambda\to JK'\lambda'})^*+(g\leftrightarrow u)],\end{aligned} \tag{28}$$

and where the Z coefficients are defined in terms of Clebsch-Gordan coefficients [27]. The partial charge-exchange cross sections are given by

$$(Q_{\mathrm{ex}}^{J\to J'})^P=\frac{\pi(2P+1)}{(2S_++1)(2J+1)k_J^2}\times\sum_{K=|J-S_+|}^{J+S_+}\sum_{l=|P-K|}^{P+K}\sum_{K'=|J'-S_+|}^{J'+S_+}\sum_{l'=|P-K'|}^{P+K'}\times|T^{Pg}_{JKl\to J'K'l'}-T^{Pu}_{JKl\to J'K'l'}|^2. \tag{29}$$

We now specialize to O^+-O and consider the total diffusion or charge-exchange cross section for initial states of a particular J. We therefore sum over the final states and define

$$Q_D^J=\sum_{J'=2}^{0}Q_D^{J\to J'}. \tag{30}$$

For comparison with the single-channel model of the preceding section, we consider the limit in which the fine-structure levels are populated in proportion to their degeneracies. Then an averaged value that can be compared with the single-channel calculations is

$$\langle Q_D\rangle=\tfrac{1}{9}\sum_{J=2}^{0}(2J+1)Q_D^J. \tag{31}$$

For this comparison, note that a given set of coupled-channel calculations is performed for a fixed value of the total energy E. E is the sum of the kinetic energy E_{kin} of relative motion of the atoms (initially, when they are infinitely separated), and the internal energy if the $O(^3P)$ is in an excited fine-structure level. For the comparison of the coupled-channel and single-channel theories, we hold the initial E_{kin} constant. Hence, in Eq. (31), $\langle Q_D\rangle$ is the average value at a particular E_{kin}, and each of the Q_D^J must be evaluated by a coupled-channel calculation for $E=E_{\mathrm{kin}}+E_J$. In practice, the cross sections were evaluated at a grid of points and then interpolated as needed using cubic splines.

IV. RESULTS AND DISCUSSION

We have performed numerical calculations of inelastic, momentum-transfer, and charge-exchange cross sections for O^+-O collisions in the energy range $E=4.0\times10^{-7}$ to 0.07 a.u. (1.1×10^{-5} to 1.9 eV). The major result of the work is the strong dependence of all of the calculated cross sections on the initial fine-structure level J of $O(^3P_J)$. In the following subsections, we first present in detail the results of the coupled-channel study, then we discuss some of the numerical techniques necessary to solve the equations reliably, and finally we compare the present theory with experiments and with other theoretical work.

A. Calculated cross sections

The analysis of the preceding section provided various cross sections for $J\to J'$ transitions, for any values of J and J'. For the cross sections $Q^{J\to J'}$, we report only the inelastic results ($J\neq J'$). The purely elastic case ($J=J'$) is less interesting and would require extra attention to the convergence of the partial wave sum over P. For the momentum-transfer cross sections, the elastic case $J=J'$ converges more easily and is easily calculated. For the energy range we considered, the inelastic cross sections $Q_D^{J\to J'}$ are much smaller than the elastic ones. In this case, we sum over the final values of J'. These results Q_D^J are the appropriate values for considering the diffusion of particular J levels of O^+ in atomic O. Finally, we also present charge-exchange cross sections.

The momentum-transfer cross sections Q_D^J are shown as a function of kinetic energy in Fig. 5. For these calculations, we performed calculations at 33 energies between $E=1.0\times10^{-5}$ and 0.07 a.u., with spacing varied between 2×10^{-5} a.u. at the lower energies to 0.01 a.u. at the highest energies. The plateau near $E=0.015$ eV in the $J=2$ curve is probably due to a Feshbach resonance. One of the adiabatic potentials shown in Fig. 1 that approaches the $J=1$ asymptotic limit clearly shows a well near $5.5a_0$. This well could cause resonance structure in the $Q_D^{J=2}$ cross sections. However, examination with a finer energy grid near this energy revealed no additional structure. The lack of sharp

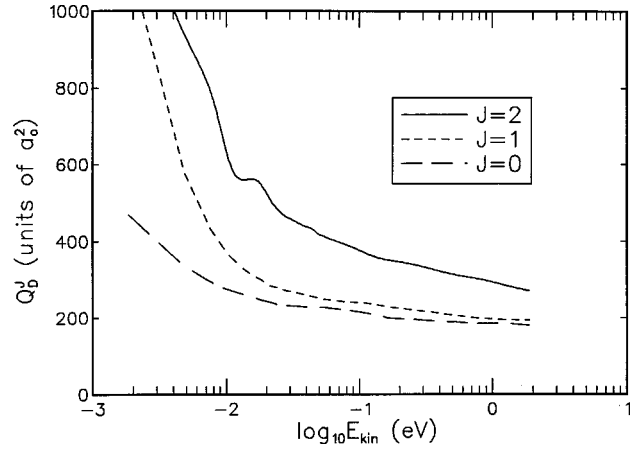

FIG. 5. The momentum-transfer (diffusion) cross section for each J, summed over all final J', as a function of the incident kinetic energy in eV.

structure may reflect that the cross sections presented have been averaged over several internal quantum numbers.

The cross sections shown in Fig. 5 exhibit a strong dependence on J: Q_D^J is typically 50% larger if the initial level is $J=2$ rather than $J=1$ or 0. The strong dependence on J can be explained qualitatively. The asymptotic form of the potential curves includes a charge-quadrupole term, which behaves as C_3R^{-3}. The value of C_3 is -0.8 a.u. for Σ states of O_2^+ and $+0.4$ a.u. for Π states. This term makes the Σ states lower in energy than the Π states asymptotically. Therefore the adiabatic potentials arising from the lowest fine-structure level ($J=2$) correlate preferentially with Σ states. However, the g-u splitting for a pair of Σ states is larger than for Π states [7]. Figure 6 shows explicitly the absolute value of the g-u splittings for each of the LS potential curves. One can see, for example, in Figs. 2 and 3 that the g-u splitting of the lower states tends to be larger than for the higher states. Previous work [1,7,8] has invariably shown that the single feature of the potentials that has the largest effect on Q_D or Q_{ex} is the rate of splitting of each pair of g-u potential curves. Faster splittings lead to larger cross sections. This same behavior persists in the coupled-channel calculations. Thus the tendency of the $J=2$ levels to correlate with Σ

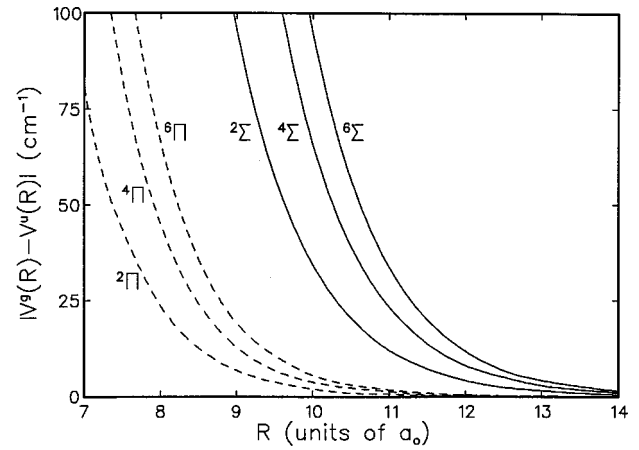

FIG. 6. Splitting of the gerade and ungerade LS potentials calculated by Stallcop *et al.* The splitting is systematically larger for Σ states than for Π states.

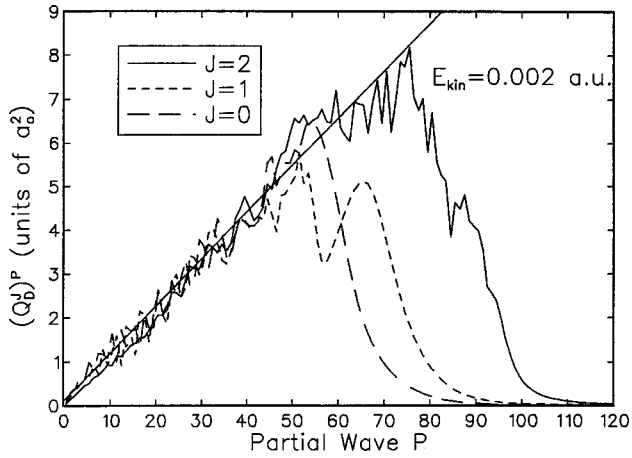

FIG. 7. Comparison of the coupled-channel results with the RPA (random phase approximation). For each level J, the total energy is chosen such that the initial kinetic energy is 0.002 a.u. (0.0544 eV). The partial cross sections $(Q_D^J)^P$ shown are the $(Q_D^{J\to J'})^P$ summed over final levels J'. In the limiting case of small impact parameters and strong coupling, the coupled-channel theory yields essentially the same results as the RPA.

potential curves and the larger g-u splitting of the Σ curves provide an explanation for the larger cross sections for $J=2$ levels.

An alternative, and somewhat more quantitative, way to interpret the difference between the Q_D^J is provided by Fig. 7. This diagram compares the behavior of the partial cross sections $(Q_D^J)^P$ for each J with the random phase approximation (RPA). The RPA, which is shown by the straight line in Fig. 7, is appropriate in the limit of strong coupling. One assumes that the phase of the sine function in Eq. (6) varies so rapidly (as a function of l) that the $\sin^2(\cdots)$ can be replaced by its average value of $\frac{1}{2}$. In the coupled-channel case, the sum is over P instead of l, and the analogous result is

$$(Q_D^J)^P=\frac{2\pi}{k^2}(P+1). \tag{32}$$

The physical meaning of this approximation is that in the strong coupling limit of O^+-O collisions, the electronic charge is equally likely to end up on either nucleus.

The excellent agreement of the coupled-channel results with the RPA for values of P up to a maximum value indicates that the RPA is a very realistic model for the strong coupling regime. The critical factor that determines the size of the Q_D is then the value of P that divides the strong coupling regime (small P) from the weak coupling regime (large P). From this viewpoint, it is clear why previous calculations have depended so strongly on the rate of the g-u splitting: this splitting determines the critical value of P. For smaller values of P, the coupling is strong enough for the RPA to be valid, and the details of the potential are not important. The present calculations show that the critical value depends on J.

Inelastic cross sections $Q^{J\to J'}$ are shown in Fig. 8. In general the inelastic cross sections $(J\neq J')$ are much smaller than for $J=J'$.

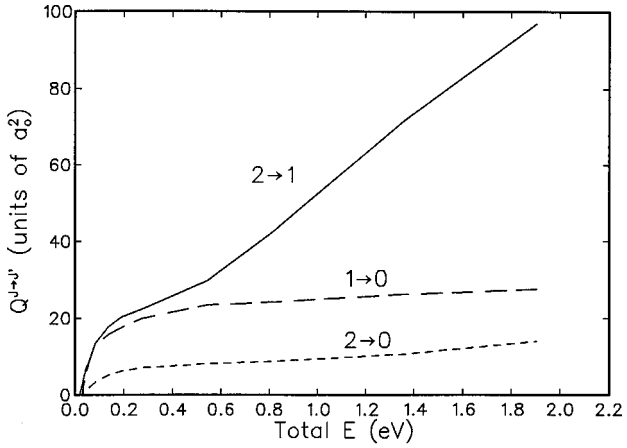

FIG. 8. Inelastic cross sections $Q_D^{J\to J'}$ as a function of the total energy.

We also present charge-exchange cross sections. From analytic considerations [1] it has been shown that in the single-channel case, one expects Q_D to be approximately twice as large as $Q_{\rm ex}$ for temperatures above about 400 K. Furthermore, the energy dependence of the cross section is expected to follow the analytic form [1]

$$(Q_D)^{1/2}=A+B\ \log_{10}E. \tag{33}$$

In Fig. 9 we present the calculated results in a way that facilitates comparison with these approximations. It can be seen that for energies above ~ 0.03 eV, twice the value of $Q_{\rm ex}$ is indeed very close to Q_D. In this energy range, $(Q_D)^{1/2}$ is also approximately a linear function of $\log_{10}E$. Both approximations break down, however, for lower energies.

B. Numerical procedures

The coupled equations were solved numerically using a method based on the log derivative algorithm [29]. We used our standard code [30], which calculates the solution in the body-fixed frame. The step size is chosen adaptively to ensure accuracy of the solution to within a prescribed tolerance. After integrating to a sufficiently large internuclear separation, we transform the solution to the space-fixed frame [25] to determine the T matrix elements by the boundary matching.

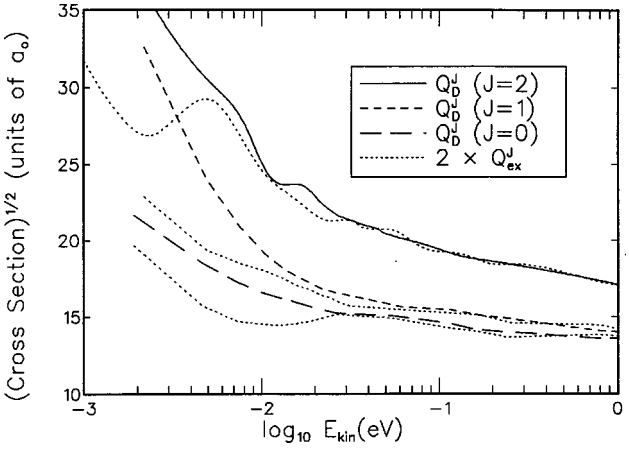

FIG. 9. Comparison of the diffusion cross sections Q_D^J with twice the charge-exchange cross sections $Q_{\rm ex}^J$. For each value of J, the dotted line for $2Q_{\rm ex}^J$ approaches the value for Q_D^J for high energies. Note that the square roots of the cross section are plotted, and the scale of the y axis does not begin at zero.

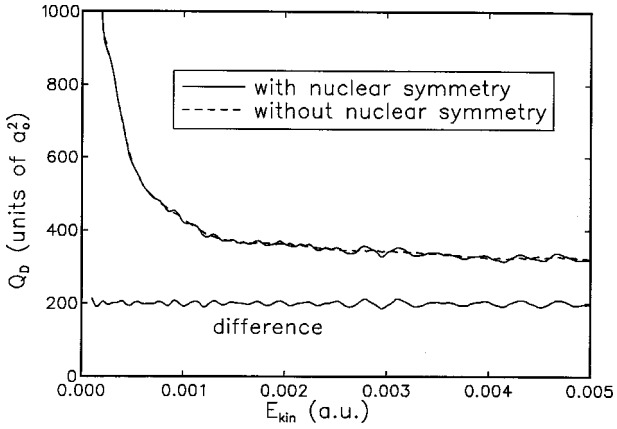

FIG. 10. Comparison of single-channel calculations that fully include nuclear symmetry with those that use the symmetrized approximation given in the text. The difference is displaced for clarity, but is shown with the same vertical scale.

Several numerical issues arose in the present investigation because of the long range behavior of the potential curves. The convergence of the partial wave sums in the single-channel calculations was discussed in Sec. III A. In addition, for each partial wave, it was necessary to integrate the equations to a sufficiently large value of R before boundary matching. For the single-channel phase shifts, we monitored the behavior of the phase shifts as a function of the angular momentum l. We were able to verify that the correct behavior was obtained for sufficiently large l, as predicted by Eq. (13). For the coupled-channel equations, we performed extensive convergence tests to make sure that the boundary matching was carried out at a sufficiently large value of R. Typical values used were $30a_0-50a_0$. Note that the results we report generally depend on the differences of T matrix elements, which converge more rapidly than the T matrix elements themselves. We checked that sufficient convergence of the partial wave sums was achieved by monitoring the asymptotic behavior of the partial cross sections (as a function of P). After evaluating the sums for all values of P up to some $P_{\rm max}$, we fit the last few terms to a power series in $1/P$. By integrating this power series from $P_{\rm max}+\frac{1}{2}$ to ∞, we could estimate the contribution to the sum of the neglected terms. Typically, we chose $P_{\rm max}$ sufficiently large that the total effect of the terms with $P>P_{\rm max}$ was on the order of 0.1% of the total cross section.

We performed numerical tests to assess the importance of nuclear symmetry effects. It was straightforward to perform single-channel calculations with and without the nuclear symmetry terms mentioned in Eq. (7). The results of these calculations are shown in Fig. 10. The results are averaged over all the $S\Lambda$ states, according to Eq. (8). Nuclear symmetry effects contribute a small oscillatory term to the total cross sections. The amplitude of the oscillations varies between about 1% and 4%. This effect is small and certainly very sensitive to the details of the potential curve. It would have a negligible effect on the cross sections convoluted over

TABLE III. Comparison of several determinations of the O^+-O collision frequency ν_{in} at $T=1000$ K divided by the oxygen density $N(O)$. Results are given in units of 10^{-10} cm^3 s^{-1}.

Date	Reference	Theoretical studies	Analysis of observations
1997	present work	9.0	
1997	Buonsanto *et al.* [17]		10.1 ± 2.2
1993	Pesnell, Omiduar, and Hogey [8]	9.2	
1991	Stallcop, Partridge, and Levin [7]	9.2	
1991	Sipler *et al.* [15]		13.7 ± 1.1
1987	Burnside, Tepley, and Wickwar [14]		12.3^{+5}_{-2}
1977	Carlson and Harper [13]		9.6
1973	Schunk and Walker [6]	7.2	
1968	Stubbe [5]	9.3	
1966	Banks [4]	7.2	
1964	Dalgarno [2]	7.3[a]	
1958	Dalgarno [1]	21.9	

[a]Determined by extrapolating experiments of Stebbings, Smith, and Ehrhardt [11].

a realistic energy distribution. We have therefore not included nuclear symmetry terms in the analysis of the coupled-channel calculations.

C. Comparison with experiment

There exist no laboratory data in the energy range of the present calculations for a direct comparison. Analysis of observations of the upper atmosphere provide information about the ion-neutral collision frequency ν_{in} for O^+-O, which is a transport coefficient defined by

$$\nu_{in}^J(T)=\frac{2}{3}\left(\frac{8kT}{\pi\mu}\right)^{1/2}N(O)\Omega_{1,1}^J(T), \tag{34}$$

where $N(O)$ is the oxygen number density and $\Omega_{1,1}^J(T)$ is the standard collision integral

$$\Omega_{1,1}^J(T)=\tfrac{1}{2}\int_0^\infty \exp(-x)x^2Q_D^J(xkT)dx, \tag{35}$$

where $x=E_{kin}/kT$, and E_{kin} is the initial kinetic energy.

In a preliminary report [10], we calculated the appropriate averages of the coupled-channel cross sections for comparison with atmospheric studies. The theoretical results are now fully consistent with the latest atmospheric studies [17]. The comparison of several studies at the representative temperature of 1000 K is summarized in Table III.

D. Comparison with other calculations

We can compare the results of the coupled-channel theory with other calculations, all of which have neglected fine structure. One comparison was discussed in a previous section (cf. Fig. 7), where the RPA was found to be reliable in the strong coupling regime. This section will focus on the low-energy behavior of the cross section.

We must average the state-to-state cross sections provided by the coupled-channel calculations to have a point of comparison with less detailed approaches. The appropriate degeneracy-weighted average of initial levels $\langle Q_D\rangle$ was given in Eq. (31). Single-channel calculations (ours and those of [7,8]) and the averaged coupled-channel calculations of $\langle Q_D\rangle$ are shown in Fig. 11. The single-channel and coupled-channel calculations agree well for energies above ~ 0.03 eV, but there are significant differences for lower energies.

We interpret these differences by analyzing in more detail the expected behavior of the cross sections in the limit $E\to 0$. This behavior is determined by the long range form of the potential curves. Equation (12) gave the asymptotic form of the potentials used in the calculations. For the single-channel calculations, in which LS potential curves are used, the value of C_3 is -0.8 a.u. for Σ states and 0.4 a.u. for Π states. The charge-quadrupole term therefore depends on the orientation of the O atom, and the average value is zero. In the single-channel model, one-third of the trajectories begin in Σ states and two-thirds begin in Π states, and the molecule is assumed to remain in the same state for the entire collision. Hence the value of C_3 used for all of the single-channel calculations is either -0.8 or 0.4 a.u., and averaging is done

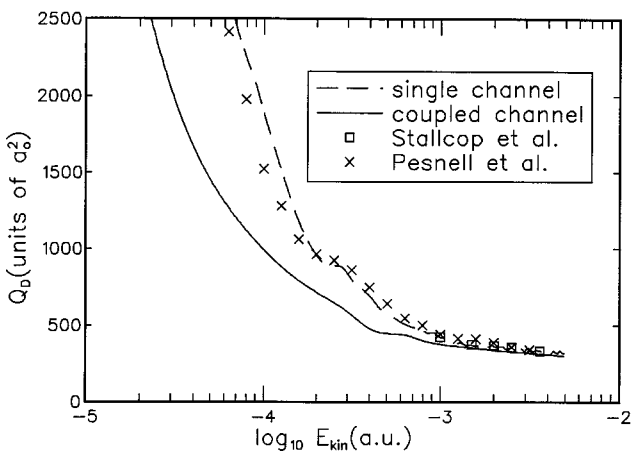

FIG. 11. Comparison of single-channel calculations with the averaged coupled-channel calculations. The coupled-channel average is calculated under the assumption that the fine-structure levels are populated statistically, that is, in proportion to their degeneracies $(2J+1)$.

TABLE IV. Values of C_3 and C_4 in atomic units for the space-fixed, coupled angular momentum representation for $P=100\frac{1}{2}$.

Channel	J	K	l	C_3	C_4
1	2	1/2	101	0.0000	−2.55
2	2	3/2	100	0.0000	−2.55
3	2	3/2	102	0.0000	−2.55
4	2	5/2	99	0.0162	−2.55
5	2	5/2	101	0.0563	−2.55
6	2	5/2	103	−0.0725	−2.55
7	2	7/2	98	−0.0221	−2.55
8	2	7/2	100	0.1448	−2.55
9	2	7/2	102	0.0802	−2.55
10	2	7/2	104	−0.2029	−2.55
11	1	1/2	101	0.0000	−2.55
12	1	3/2	100	0.0812	−2.55
13	1	3/2	102	−0.0812	−2.55
14	1	5/2	99	−0.0227	−2.55
15	1	5/2	101	−0.0788	−2.55
16	1	5/2	103	0.1015	−2.55
17	0	3/2	100	0.0000	−2.55
18	0	3/2	102	0.0000	−2.55

after the cross sections $Q_D^{S\Lambda}$ have been calculated for each symmetry. Since the cross sections at low energy are not sensitive to the sign of C_3, the cross sections reflect the average magnitudes of the C_3 coefficients of the adiabatic potential curves. In contrast, the coupled-channel method is based on a coupled angular momentum representation, in which there is some cancellation of the charge-quadrupole interaction due to contributions from different orientations of the O atom. We will show that for the coupled-channel calculations, the C_3 coefficients are much smaller and in some cases are exactly zero.

We consider now the long range form of the interaction potentials in the coupled-channel calculations. These calculations explicitly include the R^{-3} terms. However, since we perform the calculations in the BF frame, there are even longer range (R^{-2}) off-diagonal centrifugal coupling terms that cause transitions among the BF states and complicate any consideration of the asymptotic behavior of the potentials. An alternative approach is to consider the long range behavior of the potential curves in the coupled angular momentum representation (SF frame). Although we do not actually perform the numerical integration in this frame (for reasons of computational economy), we would get the same results if we did so. An advantage of considering the asymptotic interactions in the SF frame is that the centrifugal terms are diagonal, so it is easier to isolate the effect of the electronic coupling. Also, the SF frame might be considered closer to the physical situation and easier to visualize. It has been shown [27] that in the SF frame the off-diagonal terms enter in second order, and the cross sections are determined primarily by the diagonal electronic coupling matrix elements. By explicit numerical calculation, we have transformed the interaction potentials to the SF frame and evaluated the coefficients of the R^{-3} terms. These calculations verify the qualitative interpretation presented earlier. The C_3 coefficients depend on the channel, but in general are considerably smaller than the adiabatic LS values shown in Table II. Table IV gives the explicit values of the C_3 coefficients for each channel at one particular value of P. Note that the values for $J=0$ are exactly zero. One can show formally that this is an exact result for all values of P. Most values for $J=1$ and 2 are not exactly zero, but are considerably smaller than the ''pure'' Σ and Π values. Note that the value of the C_3 coefficient averaged over all the channels for a given J is zero, just as in the LS representation.

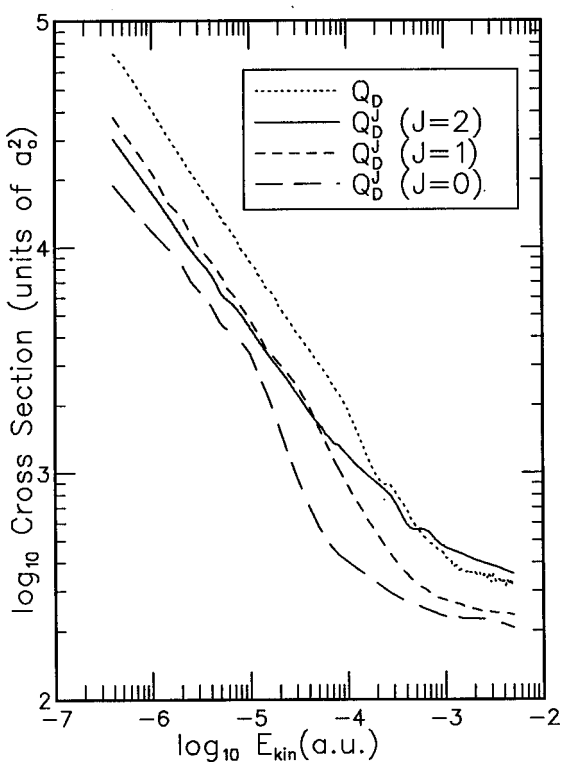

FIG. 12. The low-energy behavior of the momentum-transfer cross sections. Results from the single-channel model are compared with results for each specific J of the present coupled-channel method.

It is straightforward to evaluate the expected energy dependence of Q_D for potentials whose long range form is dominated by terms such as R^{-3} or R^{-4}. We evaluated a single-channel model based on using the RPA approximation for low partial waves and using the Born approximation for high partial waves [see Eq. (14)]. The critical value of P (or l in a single-channel model) separating these values is that value for which the argument of the $\sin^2(\cdots)$ in Eq. (6) is equal to a number of order unity. (The results are not very sensitive to this number.) Our calculations follow an approach used in standard references [24] to treat R^{-4} potentials. The result is that for C_3R^{-3} potentials, one expects

$$Q_D(E)\sim|C_3/E|^{2/3}, \tag{36}$$

and for C_4R^{-4} potentials,

$$Q_D(E)\sim|C_4/E|^{1/2}. \tag{37}$$

The value of C_3 is different for each channel, but we only use the above analysis to predict the exponent of the energy for the scaling behavior of Q_D.

Figure 12 shows the low-energy behavior of the calculated cross sections. Note the log-log scale. The slope of the single-channel calculations corresponds almost exactly to the power law dependence predicted by Eq. (36). A least squares fit to the points for $E \leqslant 2.0\times10^{-6}$ gave an exponent of -0.658. The corresponding slopes of the $J=1$ and 2 cross sections are also close to the values predicted by Eq. (36): -0.643 for $J=1$ and -0.613 for $J=2$. The slope of the $J=0$ cross section in the same energy range is -0.499, very close to the value of -0.5 predicted by Eq. (37).

The breakdown of the single-channel method occurs near a critical energy of about 0.03 eV. This energy is approximately equal to the fine-structure splitting ΔE of the $J=2$ and 1 levels. This result leads to the hypothesis that the single-channel model is reliable as long as the collision energy is larger than the splitting between the fine-structure levels. This conclusion appears plausible, since the single-channel model neglects the splitting entirely. However, we do not have a detailed model that explains the breakdown. Further studies are in progress to address this point.

V. CONCLUDING REMARKS

We have presented calculations of adiabatic potential curves for the O_2^+ molecule that include the effects of the spin-orbit operator. The curves dissociate to the three fine-structure levels of atomic oxygen. Coupled-channel calculations of the momentum-transfer and charge-exchange cross sections show a strong dependence on the initial fine-structure level. The calculated results, when averaged over a statistical distribution of initial levels, are fully consistent with the most recent results derived from atmospheric observations [16,17].

The coupled-channel calculations have enabled us to assess the accuracy of simpler approaches. The present work indicates that the single-channel method based on adiabatic potential curves is reliable for energies above about 0.03 eV. For lower energies, the dynamics of the long range charge-quadrupole (R^{-3}) interaction are not accurately handled by the single-channel method. The present study also has important implications for laboratory measurements. Our results indicate that the measured values of Q_D or Q_{ex} will depend strongly on the distribution of initial fine-structure levels.

ACKNOWLEDGMENTS

This work was supported by Grants No. ATM-9409362 and No. ATM-9632707 from the National Science Foundation. C.D.C. was supported by the NASA Delaware Space Grant Consortium and by the REU program in the Physics Department at Lehigh University. Some of the final calculations were performed by Zach Watkinson. A.P.H. acknowledges helpful conversations and correspondence with Dr. Dean Pesnell and Dr. Harry Partridge.

[1] A. Dalgarno, Philos. Trans. R. Soc. London, Ser. A **250**, 426 (1958).
[2] A. Dalgarno, J. Atmos. Terr. Phys. **26**, 989 (1964).
[3] H. Knof, E. A. Mason, and J. T. Vanderslice, J. Chem. Phys. **40**, 3548 (1964).
[4] P. Banks, Planet. Space Sci. **14**, 1105 (1966).
[5] P. Stubbe, J. Atmos. Terr. Phys. **30**, 1965 (1968).
[6] R. W. Schunk and J. C. G. Walker, Planet. Space Sci. **21**, 1875 (1973).
[7] J. R. Stallcop, H. Partridge, and E. Levin, J. Chem. Phys. **95**, 6429 (1991).
[8] W. D. Pesnell, K. Omidvar, and W. R. Hogey, Geophys. Res. Lett. **20**, 1343 (1993).
[9] C. M. Marian *et al.*, Mol. Phys. **46**, 779 (1982).
[10] A. P. Hickman, M. Medikeri-Naphade, C. D. Chapin, and D. L. Huestis, Geophys. Res. Lett. **24**, 119 (1997).
[11] R. F. Stebbings, A. C. H. Smith, and H. Ehrhardt, J. Geophys. Res. **69**, 2349 (1964).
[12] J. A. Rutherford and D. A. Vroom, J. Chem. Phys. **61**, 2514 (1974).
[13] H. C. Carlson and R. M. Harper, J. Geophys. Res. **82**, 1144 (1977).
[14] R. G. Burnside, C. A. Tepley, and V. B. Wickwar, Ann. Geophys. **5A**, 343 (1987).
[15] D. P. Sipler *et al.*, J. Geophys. Res. **96**, 21 555 (1991).
[16] M. J. Buonsanto, D. P. Sipler, and G. B. Davenport, EOS Trans. Am. Geophys. Union Suppl. **77**, S193 (1996).
[17] M. J. Buonsanto, D. P. Sipler, G. B. Davenport, and J. M. Holt, J. Geophys. Res. **102**, 17 267 (1997).
[18] J. S. Cohen and B. I. Schneider, J. Chem. Phys. **61**, 3230 (1974).
[19] J. Durup, Chem. Phys. **59**, 351 (1981).
[20] C. E. Moore, *Atomic Energy Levels*, Natl. Bur. Stand. (U.S.) Circ. No. 467 (U.S. GPO, Washington, DC, 1958), Vol. I.
[21] A. Messiah, *Quantum Mechanics* (North-Holland, Amsterdam, 1968), Vol. II.
[22] E. A. Mason and E. W. McDaniel, *Transport Properties of Ions in Gases* (Wiley, New York, 1988).
[23] W. R. Gentry and C. F. Giese, J. Chem. Phys. **67**, 2355 (1977).
[24] N. F. Mott and H. S. W. Massey, *The Theory of Atomic Collisions* (Oxford University Press, New York, 1965).
[25] R. B. Walker and J. C. Light, Chem. Phys. **7**, 84 (1975).
[26] J. M. Launay, J. Phys. B **10**, 3665 (1977).
[27] A. M. Arthurs and A. Dalgarno, Proc. R. Soc. London **256**, 540 (1960).
[28] A. P. Hickman and F. T. Smith, Phys. Rev. A **17**, 968 (1978).
[29] B. R. Johnson, J. Comput. Phys. **13**, 445 (1973).
[30] A. P. Hickman, D. L. Huestis, and R. P. Saxon, J. Chem. Phys. **98**, 5419 (1993).